Proceedings of DETC'03
ASME 2003 Design Engineering Technical Conferences and
Computers and Information in Engineering Conference
Chicago, Illinois, USA, September 2-6, 2003

DETC2003/CIE-48253

SWIRL AND COMBUSTION EFFECTS ON FLOW DYNAMICS IN LEAN DIRECT INJECTION GAS TURBINE COMBUSTION

S. Archer and A. K. Gupta*

University of Maryland
Department of Mechanical Engineering
College Park, MD 20742
*e-mail: akgupta@eng.umd.edu

Abstract

The effect of swirl and combustion are presented for a Lean Direct Injection (LDI) configuration in gas turbine combustion. Specifically, the effect of radial distribution of combustion air and swirl in a burner are examined under non-burning and burning conditions using propane as the fuel. The present study explores single swirler interaction with the use of an experimental double concentric swirl burner that simulates one swirler of a practical gas turbine combustor.

Flowfield data has been obtained using Particle Image Velocimetry (PIV) for varying swirl distributions. The flow characteristics of the resulting flowfields have been examined under lean direct injection (LDI) conditions. The affects of co- and counter-swirl have also been carried out.

Results showed that both swirl and combustion has significant effect on the characteristics of the internal and external recirculation zones. Combustion provides greater axial velocities than their counter non-combustion conditions. The counter-swirl combination resulted in smaller and more well defined internal recirculation regions. The results provide the role of swirl and combustion on the mean and turbulence characteristics of flows over a range of swirl and shear conditions between the inner and outer flow of the burner. This data provides important insights on the flow dynamics in addition to providing data for model validation and model development.

Introduction

Hydrocarbon fuels continue to be the major source of energy in all propulsion and power systems throughout the world in the foreseeable future. A major choice for converting chemical energy to thermal energy is via the combustion of hydrocarbon fuels. Therefore the world today and in the near future will continue to rely heavily on the combustion of different kinds fuel for energy. Paramount to improving combustion is to enhance efficiency, reduce the emission of pollutants, and minimize degradation of the atmosphere. Detailed insight through sufficient understanding of a combustion process can provide an insight to improve the combustion process.

Many alternatives to the traditional gas turbine are being developed and investigated. One such alternative is the fuel lean direct injection (LDI) gas turbine. Because of its ability to reduce emissions, the LDI gas turbine is considered as an alternative to the traditional gas turbine. By taking advantage of lower temperatures associated with lean combustion, reduction in NO_x formation is achieved. Fuel and air are rapidly mixed in the LDI strategy thus providing the lean combustion conditions in the combustor. In this study, the LDI strategy is extended to the combustion of propane gas, as this fuel simulates many of the characteristics of liquid fuel combustion without the added complexity of fuel droplet formation and vaporization. Mixing of fuel and air is accomplished by radially injecting fuel into the surrounding swirl induced combustion air to cause lean combustion conditions.

In order to understand the complex features associated with the non-burning and burning swirl flow conditions, detailed examination is made of the mean and turbulence characteristics of the flow under different swirl distribution conditions in the burner. Particle image velocimetry (PIV) is used to determine the flow characteristics. This diagnostic tool is instrumental for determining the turbulence, strain and vorticity associated with the flow in addition to the mean velocity that provides information on the residence time distribution in the entire flowfield. These parameters influence the emission of pollutants, including NO_x. Forthcoming legislation is making pollution regulations increasingly stringent and further reduction of pollutants level can be expected in the future. NO_x reduction can be enhanced by proper utilization of swirl, as it induces a phenomenon known as vortex breakdown, where a central recirculation zone is formed [1]. The central recirculation zone is the region of the flame that recirculates and burns hot volatile gases released from the fuel, in a low oxygen region, enabling the suppression of NO_x.

In this study co-swirl and counter-swirl flows, both without and with combustion, are examined to gain an understanding of the flow dynamics associated with the complex swirling flowfields. A common feature of many combustors is the stabilization of flames by swirl [2,3,4]. Main principle of flame stabilization is to create regions where the local velocity is equal or less than the flame propagation velocity. The characterization of the flow in a gas turbine combustor plays an important role in turbulent combustion phenomena. The understanding of complex flowfield characteristics in a burner is

necessary to understand the real flow and combustion pattern since this affects the combustion, emission and pattern factor from the combustor. These experiments also help to validate modeling and enhance model development of these complex turbulent flows.

PIV has been used in a variety of ways by several researchers. For example, PIV has been used to measure the velocity field of swirling flows from two co-rotating coal burners [5]. It has also been utilized to determine strain and stretch in flames [6]. PIV has been used to study structures of turbulent premixed flames [7,8]. It has been used to determine aerodynamic strain rate, rate of flame stretch, vorticity and strain rate during the flame vortex interaction [9]. PIV has enabled researchers to gather velocity measurements in laminar and turbulent premixed flames [10].

To the authors' knowledge there have not been any reported studies on the flowfield inside luminous flames using PIV diagnostics. This is because the second image recorded by the PIV is over-exposed in the presence of high background flame luminosity. However, recently Gupta, Linck and Archer [11] overcome this problem via the use of mechanical shutters and narrow band interference filters located in front of the CCD cameras. These shutters were allowed to close so that the luminous emission from the flame to the camera could be minimized after the second exposure. The present investigation explores the affect of swirl and combustion on the dynamics of swirl flows. Two-dimensional flowfield data are archived under non-burning and burning conditions using a double concentric swirl burner under the conditions of fuel lean direct injection (LDI).

Facility and Investigative Methodology

A double concentric swirl burner is used here that allowed systematic examination of the swirl and flow distribution in the burner. Details of the burner are described in Ref. 12. The burner allows any desired radial distribution of swirl and combustion airflow into the burner. The combustion airflow is directed through both the inner and outer annuli of the burner. Fuel is allowed to flow only through the central pipe located on the longitudinal central axis of the burner. The fuel nozzle allowed direct injection of fuel radially outwards into the surrounding combustion air via 16 holes, each of 1/16 inch diameter. The results are presented for co- and counter-swirl distribution in the outer annulus of the burner while maintaining a fixed swirl in the inner annulus.

The system used was an Integrated Design Tools (IDT) 3-D PIV system. Only the 2-D PIV data is reported here. The company's supplied proVISION^{TM} software was used to operate the IDT-1000 system and the IDT-2000 control modules with the one camera for image acquisition [13]. A SoloPIV Nd: YAG laser provided the illuminating light source. The laser is capable of firing two pulses at 15Hz. In the experiments the laser frequency was set at 5Hz, which synchronized with the camera frequency.

Basic PIV experimental steps are as follows:

1. Seeding the flow: The sub-micron size seed particles are suspended in the fluid (using a fluidized bed) to trace the motion of the fluid and provide images on the cameras.
2. Flowfield illumination: When a sheet light beam illuminates a thin slice of the flowfield, the illuminated seed particles scatter the laser sheet light beam. A camera placed normal to the sheet light beam detects the image of the particles. The sheet light beam is pulsed (switched on and off very quickly) twice at a known time interval (t).
3. Image acquisition: The first pulse of the laser freezes images of the initial positions of seeded particles in the flow and forms the first image frame of the camera. The data from this frame is transferred to a buffer and then the PC. The camera is then exposed to second image frame of the light scattered by the particles from the second pulse of laser light. There are thus two camera images, the first showing the initial positions of the seeded particles in the frame and the second image showing their next position after a known time interval due to the motion of the flowfield.
4. Vector processing: The two-recorded images are then processed to determine the velocity vector map and turbulence characteristics of the flowfield. This involves dividing the camera frames into small areas called interrogation regions.

In the experiments two-particle seeders are used to supply the titanium dioxide tracer particles to the combustion airflow so that the inner and outer annulus could both be seeded sufficiently and independently. Also a single CCD camera frame is double exposed to enhance the accuracy of velocity measurements in the turbulent flow. Double exposing a single frame allows for smaller pulse separations, so that they are not constrained by the speed of the camera used for image acquisition thus allowing for less tracer particles to escape the recorded image frame. Two CCD cameras with active pixel array of 1280 x 1024 are used (sharpVISION^{TM} 1300-DE, model Sony ICX085AL CCD). Both cameras are equipped with a bandpass filter having center wavelength of 532nm that has a 50% transmission with a bandwidth of 0.87nm. The system also uses a novel mechanical shutter design that allows data acquisition in luminous flames. The mechanical shutter allowed significant reduction in the amount of light exposed to the CCD sensor with the result that the second image needed for processing is not saturated. The proVISION^{TM} software is used to acquire and process the images. Tecplot is used for presentation of the data in the desired graphical form.

Results and Discussion

The PIV provided information on the mean and turbulence characteristics of the flow under non-burning and burning conditions. The results presented here are the average fields for axial and radial components of velocity, rms components for axial and radial velocity, vorticity, and axial strain. The results are presented for a swirl combination of 30/50, 30/-50, 45/50 and 45/-50 in the inner and outer annuli of the burner, respectively under non-burning conditions. The results are also obtained for 45/50 and 45/-50 swirl combination under combustion conditions. These combinations provided the role of swirl and combustion on the dynamics of the flow under different shear flow conditions between the inner and outer annulus of the burner. The results obtained on the dynamics of turbulent swirl flows for different LDI conditions under non-burning and burning conditions are presented in the following.

Non-burning Case

The results obtained for axial and radial velocity for a co-swirl combination of 30/50 are shown in Figs. 1 to 4, while that for a counter-swirl combination of 30/-50 are shown in Figs. 5 and 6. The length of the velocity vector provides the total velocity (axial plus radial) while the horizontal bar above the figure shows the velocity associated with the specific component of velocity (axial or radial). These results show that for the non-burning case the size of the central recirculation region varies with the radial distribution of swirl. The co-swirl configuration shows a narrower central recirculation region. This co-swirl

combination produces a more well-defined and consistent zone of flow separation. Also there is no evidence of the downstream stagnation location in the co-swirl vector plots. This can be directly observed from the velocity slices shown at different locations downstream of the flow regime, see Figs. 3 and 4. Similar phenomenon is observed for the 45/50 and 45/-50 swirl combination in the burner, see Figs. 7 - 10. Changing the amount of shear between the flows from the inner and outer annulus of the burner, obtained by changing the swirl vane angle from 30° to 45° decreased the width and length of the central recirculation zone. This inner swirl change also resulted in less radial spreading. A comparison of Figs. 2 and 7 (co-swirl) with Figs. 5 and 9 (counter-swirl) reveals a thinner recirculation zone for inner annulus swirl vane angle of 45° as compared to the 30° inner swirler case. The co-swirl configurations observed in the vector plots do not impact the flowfields with as much recirculation strength as compared to the counter-swirl configuration.

From theses observations it is apparent that the radial pressure gradient (responsible for centrifugal force) is greater for a co-swirl configuration. The radial pressure gradient is given by:

$$\frac{dp}{dr} = \rho * \frac{u_t^2}{r} \qquad (1)$$

where,
p = pressure
r = radius
ρ = density
u_t = tangential velocity

The radial velocity vector plots (Figs. 4, 6, 8 and 10) show the presence of negative radial velocity in the upper recirculation region. The negative radial velocity shows that flow is entrained into the recirculation zone. The increase of swirl vane angle in the inner swirler causes a significant amount of reverse flow near to the burner exit plane. This reverse flow zone was also evident from the direct flame photographs that supported the visible bottlenecks of the flames with the inner swirler vane angle greater than 30°.

The processed vector plots show that the strength of the radial velocity and the negative axial velocity helps to create the bottleneck feature observed in the direct flame photographs. The increase in inner swirler vane angle increases tangential momentum imposed on the flames. This can also be concluded based on the radial pressure gradient given in equation 1. The radial pressure gradient depends greatly on the tangential velocity (u_t). The vector plots also display higher velocity components near the edges of the flow. This is a direct result of the influence of swirl, which enhances radial spreading. Stronger swirl achieved with higher swirl vane angle enhances the radial spreading for the co-swirl case. However for the counter swirl case higher turbulence levels are achieved at the interface between the flows from inner and outer annuli of the burner.

Figures 5 and 9 show increased compactness of the central torroidal recirculation zone with increased swirl vane angle in the inner annulus. The central recirculation zone is the result of a highly non-steady phenomenon, called the vortex breakdown. The recirculation zone and the phenomenon of vortex breakdown can substantially influence distribution of the velocity components.

Vorticity provides an important aspect of these complex flowfields. The vorticity is calculated using the following equation.

$$\Omega_z = \frac{du}{dy} - \frac{dv}{dx} \qquad (2)$$

where,
Ω_z = vorticity
v = axial velocity (in the direction of the flow)
u = radial velocity

The vorticity generated in the non-burning flowfields (see Figs. 11, 12, 13, and 14) is seen mostly in the shear layer region and in the area where the swirling flows from the inner annulus interact with the flow from the outer annulus. This observation supports what is expected in terms of flow movement and areas of the greatest interaction between the fuel and air. This also supports the idea of eddies being created in the shear layer region that move throughout the flame possibly driving the pollution formation. The vortical structures depicted by the vector plots also support the notion that mixing is increased with a counter-swirl configuration due to the higher rms axial and radial velocity associated with the flow. The counter-swirl vorticity vector plots shown in Figs. 11 and 12 reveal wider vorticity regions that are dense and compact, thus providing better mixing between the fuel and air streams. The co-swirl vorticity vector plots are shown in Figs. 13 and 14. In co-swirl (45/50, 30/50) and counter-swirl (45/-50, 30/-50) arrangements, the stronger vorticity regions lie outside the central reciruclation zone. This emphasizes the phenomenon of vortex breakdown that is responsible for creating these recirculation zones. The counter-swirl flowfields have wider and stronger vorticity regions and a somewhat weaker (meaning shorter) central recirculation zone as compared to the co-swirl arrangement.

Axial strain is also an important aspect of the swirling flowfield. The axial strain is given by:

$$S_y = \frac{du}{dy} \qquad (3)$$

where,
S_y = axial strain
u = radial velocity

The axial strain was calculated for each of the swirling flowfields examined here. As expected, the regions of strong axial strain are adjacent to the regions of strong vorticity. There are high velocity gradients at or just above the exit plane and near to the flow interface region between the inner and outer annulus. For the counter-swirl (45/-50) case the regions of axial strain moves toward the downstream stagnation location. This seems reasonable in that the velocity at this location approaches towards zero, as expected from the high gradients in this area. By comparing the axial strain and vorticity plots for the counter-swirl (45/-50) case at the upstream location plane, it can be seen that the region of high strain is outside the regions of vorticity. Axial strain vector plots are given in Figs. 15 and 16 for swirl cases 45/-50 and 45/50, respectively. However, further downstream of the flow, the strain regions are inside the regions of vorticity. This observation is the result of the opposing movement caused by the flows from inner and outer swirlers. The effect of co-swirl (45/50) differs from counter-swirl (45/-50) arrangement having greater strain values (both magnitude and size) at upstream locations of the flow. There are regions of high axial strain further downstream and further out towards the edges of the flow. The co-swirl case enhances radial spreading and consequently the angular momentum. Angular momentum is given by:

$$M_{\varphi} = \int u_t * r * \rho * 2 * \pi * r dr \qquad (4)$$

where,

M_{φ} = angular momentum

r = radial distance

An examination of this equation suggests that angular momentum is dependent on the integration of several terms. The co-swirl condition lends itself to give a wider range of tangential and radial velocities. The vorticity regions are also moved radially outwards for the co-swirl combination case of 45/50. The higher magnitudes of vorticity and axial strain suggest that there is less influence of vortex breakdown in the co-swirl case. This can be clearly seen from the results of the elongated recirculation zone in the axial velocity plots.

The high axial strain and high axial rms velocity regions overlap for both the co-swirl (45/50) and counter-swirl (45/-50) vector plot cases. High values of axial strain can be seen in the shear layer region for the 45/-50 swirl distribution case. This combination results in better mixing at the interface between the shear layer regions of the flow located near to the interface between the inner and the outer annulus of the burner.

Burning Case

In the burning flowfield cases, an overall increase of the velocity vector occurs, see Figs. 17-24. Thus one can conclude that combustion enhances an increase of both axial and radial velocity of the flow. The exothermic reactions cause the hot gases created in the flame environment to travel faster than the corresponding fluid under non-combustion conditions. This is because the hotter gases have a lower density and thus the higher momentum gained at the reaction zone results in greater velocity of the flow. Furthermore, combustion increases the size of the overall recirculation region (see Figs. 17 and 19) as compared to that observed in the non-burning case (Figs. 7 and 9). Heat release from combustion causes flow expansion in the combustion case. The flame environment caused the observed flowfield to become more dynamic. The complex flow dynamics observed in the hybrid luminous and blue flames allows one to gain further insight into the combustion behavior. The results provide the clear enhancement of recirculation regions with combustion for the swirl combinations examined here. For both non-burning flowfield (Fig. 7) and combustion (Fig. 17) cases no strong downstream stagnation point was observed for co-swirl combination. The counter-swirl configuration (Fig. 19) shows a stagnation point and a more compact recirculation region. These compact and intense recirculation regions observed for the counter-swirl configuration are attributed to the high strain that occurs as a result of the interactions between flows from inner and outer annuli of the burner.

The strain produced for the counter-swirl configuration (Fig. 24) is stronger, thus causing the flame to have a greater and stronger recirculation region. Negative radial velocity (see Figs. 18 and 20) suggests that flow is entrained into the recirculation zone. This is also present in the non-combusting case (Figs 4, 6, 8, and 10). In the flame environment (Figs. 21 and 22) the higher vorticity levels are widely seen near to the regions of the shear layer and near to regions of swirl interaction located between the inner and outer annulus of the burner. The co-swirl flame flowfield (Fig. 21) produced a thin region of vortical structures as compared to that for the counter-swirl flame case (Fig. 22). The vorticity associated with the co-swirl case (Fig. 21) is greater than that for the counter-swirl case, Figs 22. This is a direct result of the flow interaction from the inner and outer swirlers that have flows in the co- and counter directions. The vortical structures could lead to the emission of pollutant species that are produced and not consumed because of the speed in which they are traveling. Combustion shifts the region of vorticity further towards the edges of the flow. Combustion seems to have the effect of moving the dynamic regions of the flow radially outwards because of the exothermic reactions that transports the flow radially outwards. In the case of a jet flame, there needs to be diffusion of the air and fuel for combustion to take place. The LDI flame under investigation essentially behaves like a totally premixed flame. The high axial strain regions for the 45/50 combusting case (Fig. 23) moves to the upstream region in the central recirculation region of the flow with the 45/-50 swirl combustion case (compare Fig. 23 with Fig. 24). There are high gradients near the stagnation point in the combusting flowfield case, similar to that found for the non-burning case (Fig. 15).

Conclusions

The PIV images have been successfully acquired in both non-burning and hybrid color flames that showed luminous and blue regions in the flames. The 2-D images of mean and rms velocity as well as vorticity and strain rates of the flow under non-burning and combustion conditions allowed examination of the complex flowfield dynamics associated with swirl assisted combustion. The data provides the direct effect of swirl distribution in a burner and combustion on the dynamics of the flow under LDI conditions. The results show that co-swirl configurations can lead to a more elongated flowfield as compared to the counter-swirl case. Also the flames obtained with the co-swirl configuration could possibly provide a more symmetrical and stable flame. This may be due to the creation of a less energetic and dynamic flowfield. The data provided the direct effect of swirl strength and the swirl distribution in the burner on the flowfield and its effect on combustion. This information is critical for the design of high efficiency and low emission LDI combustors.

Acknowledgments

This research was supported by NASA Glenn Research Center and NASA URETI. Technical discussions with Mr. Bob Tacina and Dr. Chi-Ming Lee are gratefully acknowledged.

References

1. Gupta, A. K., and Lilley, D.G. and Syred, N.: Swirl Flows, Abacus Press, Tunbridge Wells, England, 1984.
2. Halthore, R.N. and Gouldin, F.C., "Laser Scattering Measurements for Gas Densities in a Swirling flow combustor, AIAA Journal 24, pp. 1129-1136, 1986.
3. Jones, W.P. and Wilhelmi, J., "Velocity, temperature and Composition Measurements in a Confined Swirl Driven Recirculating Flow", Combustion Science and Technology 63, pp. 13-31, 1989.
4. Bicen, A.F., Tse, D.G.N., and Whitelaw, J.H., "Combustion Characteristics of a Model Can-Type Combustor", combustion and Flame 80, pp. 111-125, 1990.
5. Aroussi, A., Kucukgokoglan, S., Menacer, M., Pickering, S.J., "PIV Measurements of Swirling Flows From Two Adjacent Burners", 9th International Symposium on Flow Visualization, Heriot-Watt University, Edinburgh, Scotland 2000.
6. Nie, J.X., Yeboah, Y.D., Bota, K.B., and Bai, T., "Laser Doppler Velocimetry and Particle Image Velocimetry Measurements of Premixed Methane-Air Flames and their

comparisons", 3RD ASME/JSME Joint Engineering Conference, San Francisco, CA, USA, 1999.
7. Yeboah, Y.D., Nie, J.X., Bota, K.B., Bai, T., and Ross, H.D., "Particle Image Velocimetry Measurements of Premixed Methane-Air Flames," The Proceedings of 1998 ASME Fluids Engineering Division Summer Meeting, Washington, DC, FEDSM98-5267, 1-25, 1998.
8. Yeboah, Y.D., Nie, J.X., Bota, K.B., Bai, T., and Ross, H.D., "Particle Image Velocimetry Measurements of Premixed Methane-Air Flames and its Numerical Modelling," 1998 AIChE Annual Meeting, Miami, FL, Paper 230-e, 15-20, 1998.
9. Driscoll, J.F., Sutkus, D.J., Roberts, W.L., Post, M.E., and Goss, L.P., "The Strain Exerted by a Vortex on a Flame Determined from Velocity Field Images", Combust. Sci. and Tech., Vol 96, pp.213-229, 1994.
10. Mungal, M.G., Lourenco, L.M., and Krothapalli, A., "Instantaneous Velocity Measurements in Laminar and Turbulent Premixed Flames Using On-Line PIV", Combust. Sci. and Tech. Vol 106 pp. 239, 1995.
11. Gupta, A. K., Linck, M. and Archer, S: A New Method to Measure Flowfield in Luminous Spray Flames, Submitted to J. Propulsion and Power, November 2002.
12. Qi, S., Gupta, A. K. and Lewis, M. J., "Effect of Swirl on Temperature Distribution in Premixed Flames"' 35th AIAA Aerospace Sciences Meeting & Exhibit, 1997, Paper No. 97-0373.
13. IDT, proVISION™, software release 2.01, Particle Image Velocimetry User Manual, Tallahassee, FL, Revised August 2002.
14. Archer, S. and Gupta, A. K.: Effect of Swirl and Combustion on Flow Dynamics in Lean Direct Injection Gas Turbine Combustion, AIAA Aerospace Sciences Meeting, Reno, NV, Jan. 6-9,2003, paper no. 2003-1343.

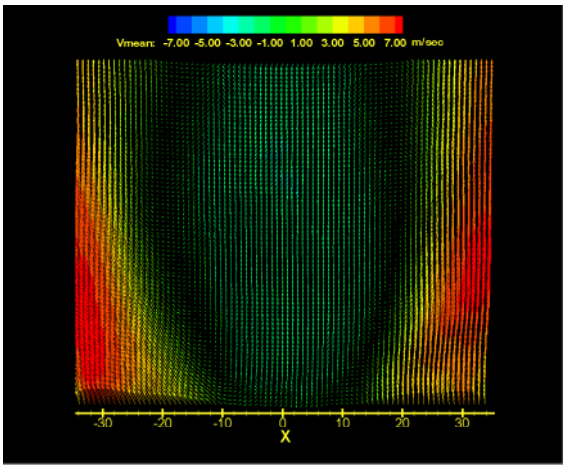

Co-Swirl: An1: 30°, An2: 50°

Fig. 1. Axial velocity for 30/50 co-swirl case under non-burning condition.

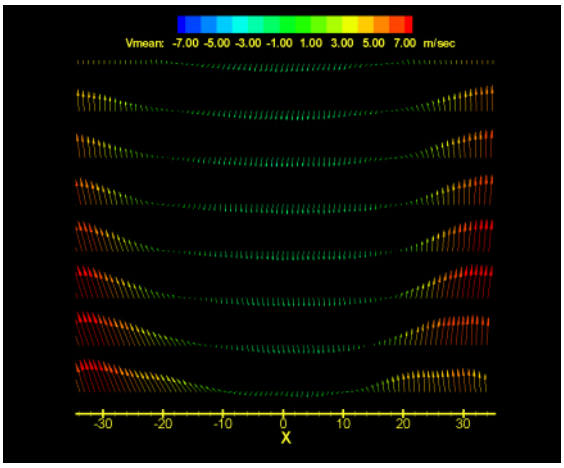

Co-Swirl: An1: 30°, An2: 50°

Fig. 2. Profiles of axial velocity for 30/50 co-swirl case under non-burning condition.

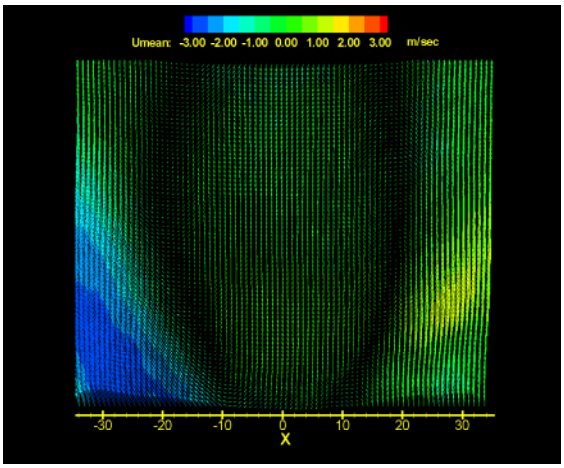

Co-Swirl: An1: 30°, An2: 50°

Fig. 3. Radial velocity for 30/50 co-swirl case under non-burning condition.

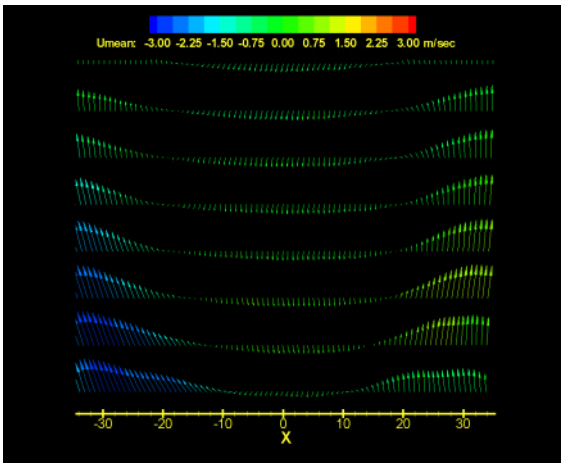

Co-Swirl: An1: 30°, An2: 50°

Fig. 4. Profiles of radial velocity for 30/50 co-swirl case under non-burning condition.

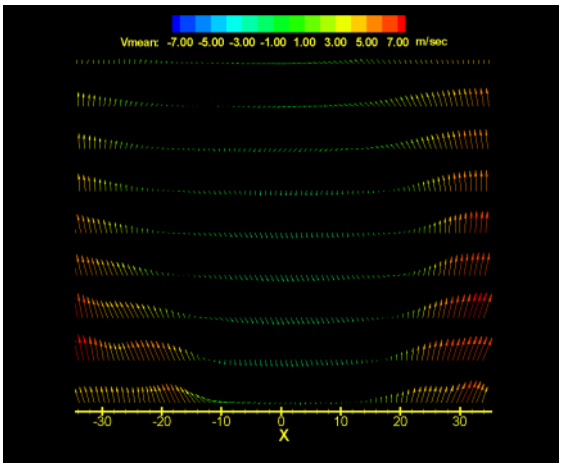

Counter-swirl: An1: 30°, An2: -50°

Fig. 5. Profiles of axial velocity for 30/-50 counter-swirl case under non-burning condition.

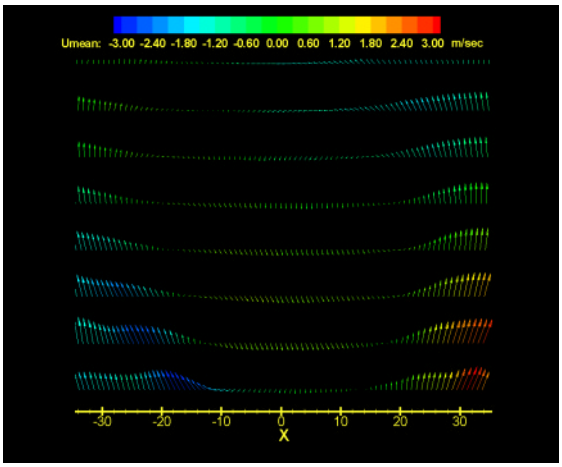

Counter-swirl: An1: 30°, An2: -50°

Fig. 6. Profiles of radial velocity for 30/-50 counter-swirl case under non-burning condition.

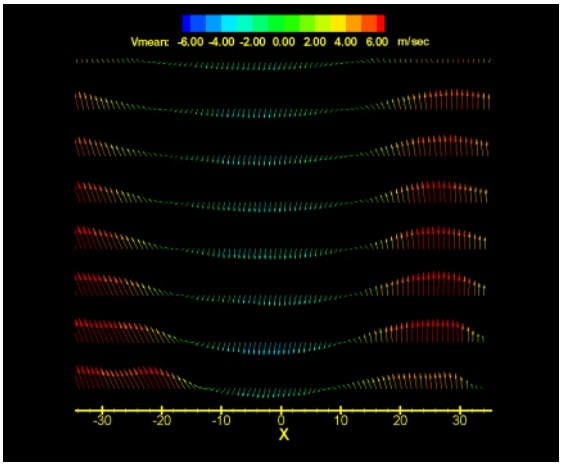

Co-swirl: An1: 45°, An2: 50°

Fig. 7. Profiles of axial velocity for 45/50 co-swirl case under non-burning condition.

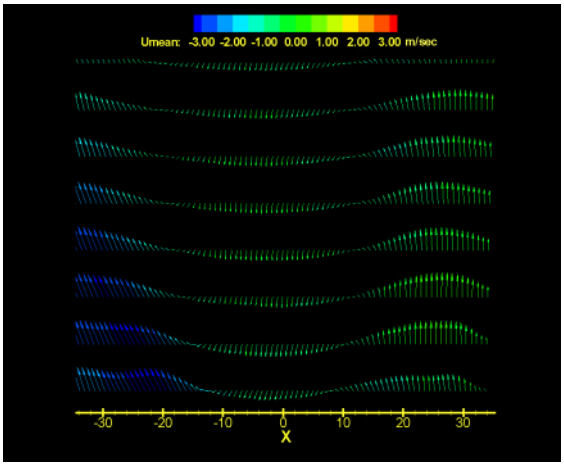

Co-swirl: An1: 45°, An2: 50°

Fig. 8. Profiles of radial velocity for 45/50 co-swirl case under non-burning condition.

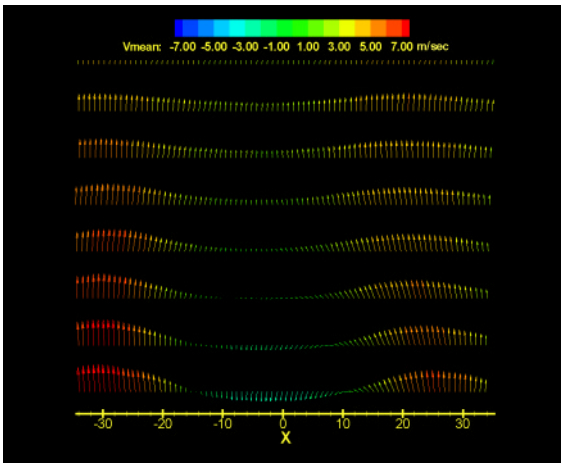

Counter-swirl: An1: 45°, An2: -50°

Fig. 9. Axial velocity for 45/-50 counter-swirl case under non-burning condition.

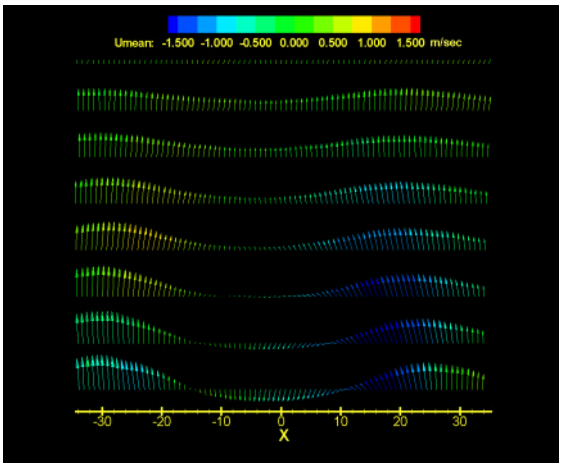

Counter-swirl: An1: 45°, An2: -50°

Fig. 10. Radial velocity for 45/-50 counter-swirl case under non-burning condition.

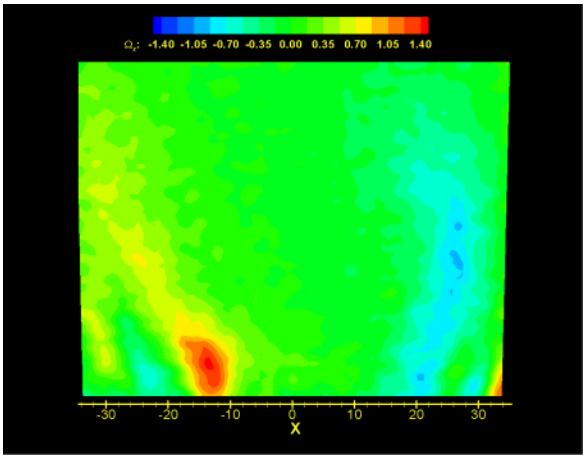

Counter-swirl: An1: 30°, An2: -50°

Fig. 11. Distribution of vorticity for 30/-50 counter-swirl case under non-burning condition.

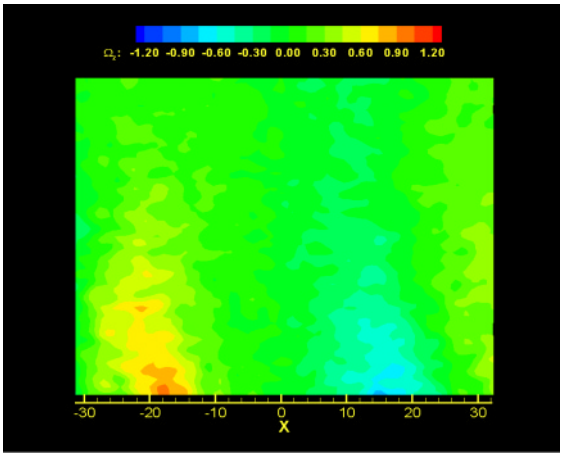

Counter-swirl: An1: 45°, An2: -50°

Fig. 12. Distribution of vorticity for 45/-50 counter-swirl case under non-burning condition.

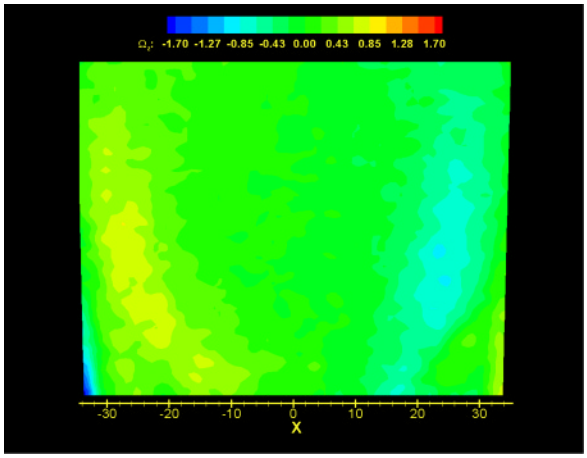

Co-swirl: An1: 30°, An2: 50°

Fig. 13. Distribution of vorticity for 30/50 co-swirl case under non-burning condition.

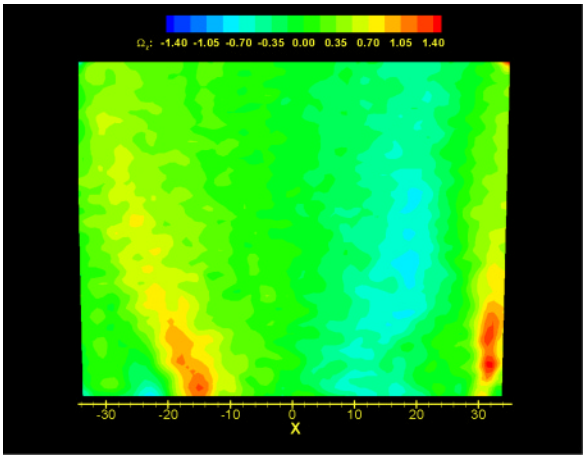

Co-swirl: An1: 45°, An2: 50°

Fig. 14. Distribution of vorticity for 45/50 co-swirl case under non-burning condition.

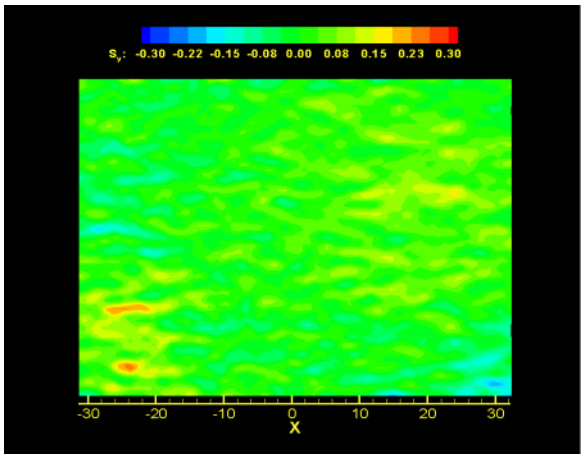

Counter-swirl: An1: 45°, An2: -50°

Fig. 15. Distribution of axial strain for 45/-50 counter-swirl case under non-burning condition.

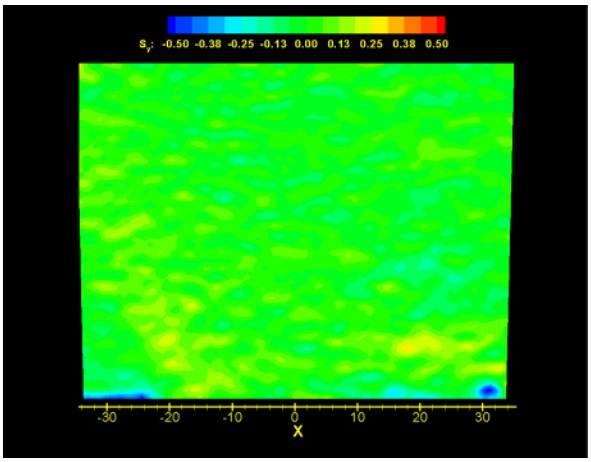

Co-swirl: An1: 45°, An2: 50°

Fig. 16. Distribution of axial strain for 45/50 co-swirl case under non-burning condition.

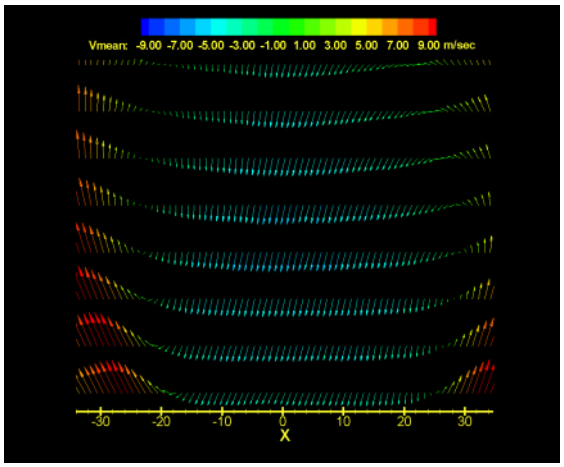

Co-swirl: An1: 45°, An2: 50°

Fig. 17. Profiles of axial velocity for 45/50 co-swirl case under burning condition.

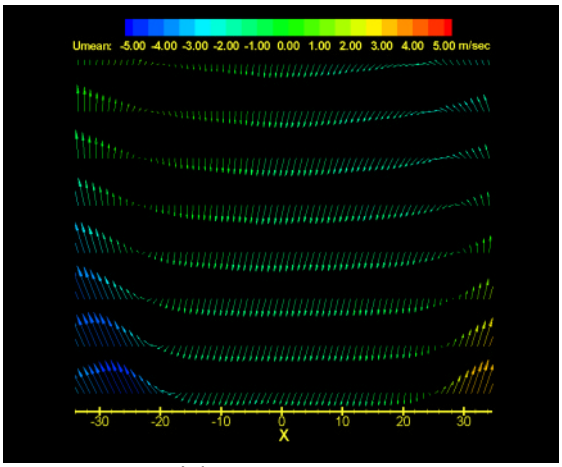

Co-swirl: An1: 45°, An2: 50°

Fig. 18. Profiles of radial velocity for 45/50 co-swirl case under burning condition.

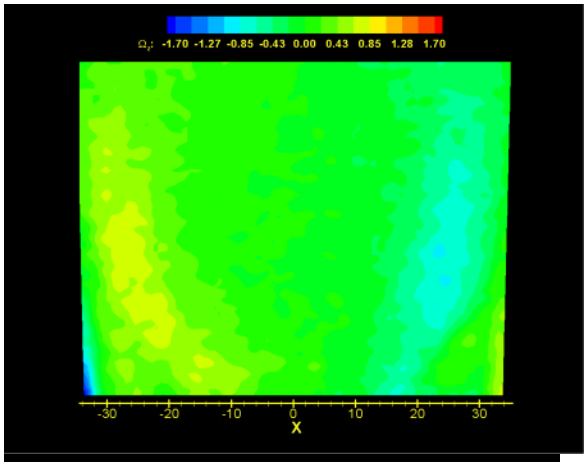

Counter-swirl: An1: 45°, An2: -50°

Fig. 19. Profiles of axial velocity for 45/-50 counter-swirl case under burning condition.

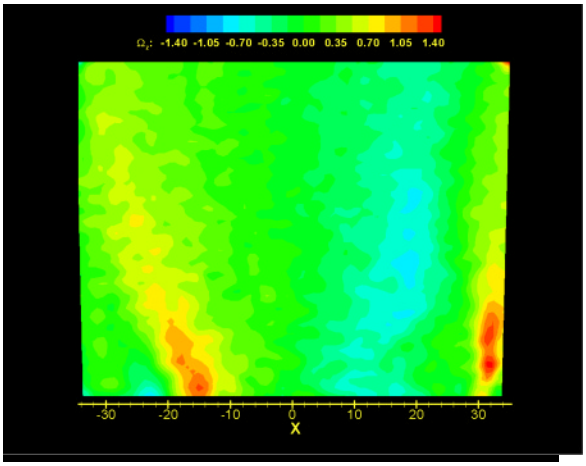

Counter-swirl: An1: 45°, An2: -50°

Fig. 20. Profiles of radial velocity for 45/-50 counter-swirl case under burning condition.

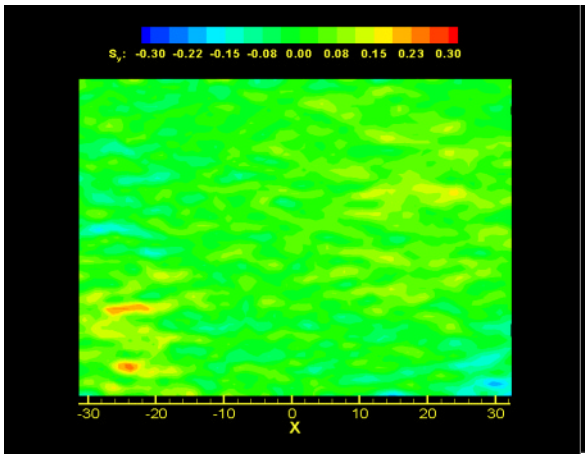

Co-swirl: An1: 45°, An2: 50°

Fig. 21. Distribution of vorticity for 45/50 co-swirl case under burning condition.

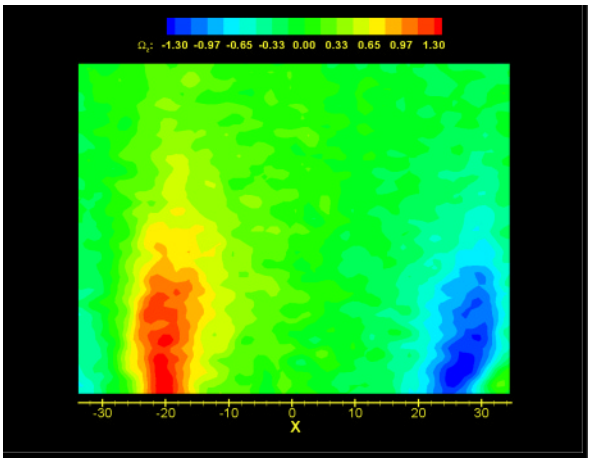

Counter-swirl: An1: 45°, An2: -50°

Fig. 22. Distribution of vorticity for 45/-50 counter-swirl case under burning condition.

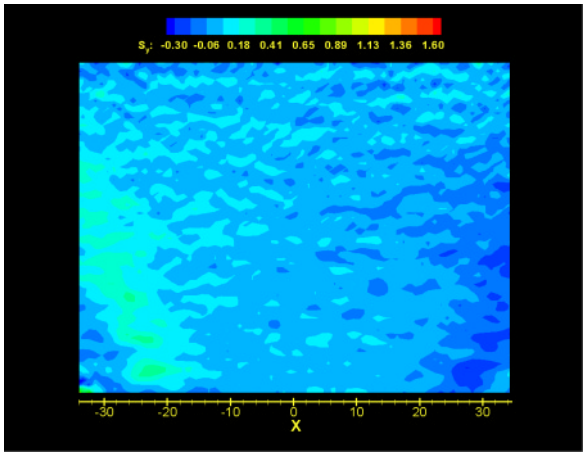

Co-swirl: An1: 45°, An2: 50°

Fig. 23. Distribution of axial strain for 45/50 co-swirl case under burning condition.

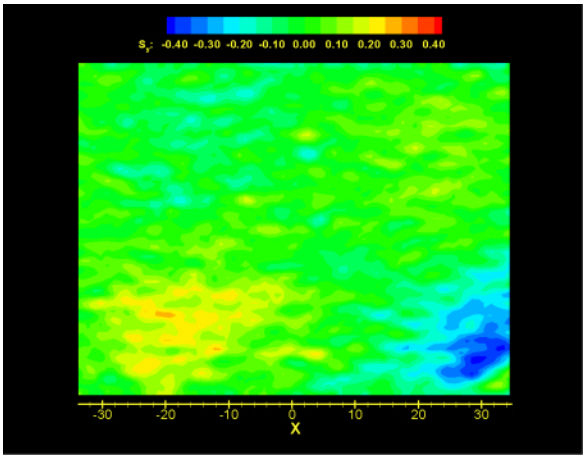

Counter-swirl: An1: 45°, An2: -50°

Fig. 24. Distribution of axial strain for 45/-50 counter-swirl case under burning condition.